Future Technology
Open Access Journal
ISSN 2832-0379

February 2027| Volume 06 | Issue 01 | Pages 67-76

Journal homepage: https://fupubco.com/futech

https://doi.org/10.55670/fpll.futech.6.1.6

Future Publishing LLC

Article

Digital-twin-oriented urban material planning for seasonal heat mitigation: a static Xujiahui case study

Wang Zhongzhuang, Cristina Amor Rosales, Anton Louise De Ocampo*

College of Engineering, Batangas State University, Batangas City, Philippines, 4200

ARTICLE INFO

Article history:
Received 16 June 2026
Received in revised form
27 October 2026
Accepted 21 November 2026

Keywords:
Urban heat mitigation, Digital twin, Constrained optimization, Surrogate model, Radiant temperature

*Corresponding author
Email address:
antonlouise.deocampo@ieee.org

DOI: 10.55670/fpll.futech.6.1.6

ABSTRACT

Material choice is one of the few levers a city has against summer radiant exposure, but a surface chosen for August remains in place in January. This study builds a digital-twin-oriented planning framework for 63 parcels in Xujiahui, Shanghai, China, combining a simplified radiative model with an Extreme Gradient Boosting (XGBoost) surrogate and a physics-constrained genetic algorithm (PC-GA). Corrected exterior-ground sky-view factors and 14 source-linked optical material analogs yield 37,800 synthetic radiative labels. On spatial and material holdouts, the surrogate reaches summer root mean square errors (RMSE) of 0.495 to 1.240 °C against the radiative generator. Across 30 seeds at 4,860 evaluations per run, PC-GA attains the lowest mean surrogate summer objective, 55.703 ± 0.253 °C, and the highest three-objective hypervolume, 0.592, of the four methods compared. Direct evaluation under 30 shared synthetic forcing realizations gives a summer-oriented plan 1.484 °C of cooling in mean radiant temperature (MRT). The same plan lowers winter MRT by 1.819 °C, a seasonal cost. Cooling survives every sky-view factor perturbation tested. Observational calibration and operational feedback remain to be built.

1. Introduction

Urban surface materials influence outdoor radiant exposure, but how much they matter at street level depends on the surrounding geometry, the season, and what can actually be built [1–3]. Mitigating the urban heat island (UHI) through material choice therefore requires a representation that captures geometry, material properties, and buildability in one object. This paper builds that representation for a static case in Xujiahui, Shanghai, China, and uses it to search for feasible material plans, while setting out what an observation-driven version would still need. Thermal digital twins already bring spatial and environmental information together [4], and surrogate models reduce the cost of scoring alternative microclimate scenarios [5,6]. The difficulty comes after prediction, because a predicted thermal field becomes a material plan only when the physical properties of each candidate surface, the limits imposed by construction and adjacency, and the seasonal consequences of the choice are carried through the same calculation. The workflow described here keeps them attached from representation through to constrained search.

The paper sets out four objectives: (1) to establish geometry-linked material representations for walls, roofs and pavements; (2) to measure surrogate accuracy not only on random rows but on spatial and material holdouts, which are the splits that expose transfer failure; (3) to compare constrained optimization methods at an identical evaluation budget, so that the comparison turns on the method itself; and (4) to test how far the predicted summer cooling survives uncertainty in the ground sky-view factor (SVF). Sensor assimilation and operational feedback are treated throughout as extensions that have not been validated here. The work covers 63 urban parcels and 37,800 synthetic radiative labels, with every optimization experiment repeated over 30 seeds. Ground-receptor SVF is recalculated, and source-linked material properties are carried into the radiative model. Selected plans are then re-evaluated by direct radiative calculation and tested against SVF perturbation; the seasonal trade-off reported later rests on these two steps. Section 2 sets out the related work and the gap. Section 3 gives the framework and the methods, Section 4 the results and the sensitivity analyses, and Section 5 the conclusions.

Abbreviations

DSM	Digital surface model
GA	Genetic algorithm
HTTP	Hypertext Transfer Protocol
IoT	Internet of Things
MAPE-K	Monitor, Analyze, Plan and Execute over Knowledge
MQTT	Message Queuing Telemetry Transport
PC-GA	Physics-constrained genetic algorithm
RMSE	Root mean square error
SVF	Sky view factor
UHI	Urban heat island
XGBoost	Extreme Gradient Boosting

Nomenclature

D(t)	Digital twin state at time t
X	Global intervention vector
F1	Summer mean radiant-temperature objective (°C)
F2	Negative winter mean radiant-temperature objective (°C)
F3	Nominal unit-area cost index
Ω	Feasible design set under implemented rules
Knb	Neighborhood shortwave-reflection proxy
st	System state vector at time t
Kt	Assimilation gain at time t
Ri	Vulnerability weighted risk index of entity i
δz,t	Zone level discrepancy between prediction and assimilation
N	Number of parcels in the case study (63)
s	Ground sky view factor at a parcel
α	Surface reflectance; subscripts w, r and p denote wall, roof and pavement
ε	Surface emissivity
ψ	Sun exposure switch in the radiative model
σ	Stefan–Boltzmann constant
θ	Radiative-model parameters
β	Fitted surrogate parameters
h_i	Height to square-root-of-footprint ratio of parcel i
A_i	Projected footprint area of parcel i (m^2)
κ_i	Nominal cost score of the material assignment of parcel i
Δ	Plan change count between successive material plans

2. Related work and research gap

2.1 Thermal twins and surrogate-assisted design

Urban thermal digital twins combine spatial representations with simulation and environmental observations, supporting thermal assessment and decision-making [4]. Surrogate-assisted methods cut the cost of evaluating building and microclimate design alternatives [5, 6]. A third strand updates modeled urban thermal states by assimilating meteorological measurements [7], which is the role the sensing and correction interfaces described later would play. This study applies these approaches at the parcel level, tying material decisions to modeled seasonal response through explicit feasibility constraints and multi-objective search.

2.2 Scope of the study

The evaluated workflow starts from building footprints and estimated heights, derives radiative descriptors from them, generates synthetic mean radiant temperature (MRT) responses, trains surrogate models on those responses, and optimizes the material assignment. Sensor monitoring, data assimilation, and planner approval are specified in Section 3 but were not implemented or tested.

3. Material and methods

3.1 Proposed architecture

Figure 1 shows the framework as four layers: data acquisition, urban representation, thermal prediction with optimization, and decision support. This study validates everything in the middle two layers and in the search that follows them: geometry-based modeling, radiative evaluation, surrogate prediction, and constrained material optimization. Observation assimilation and human-in-the-loop decision-making are drawn as extensions for a later deployment. In such a deployment, each prediction request would carry its geometry and model versions, the identifier of the meteorological forcing used, and the material configuration being scored. Each optimization output would return the seasonal thermal objectives, the nominal cost index, any constraint violations, and the provenance of the data behind them, so that two candidate interventions could be compared on the record before a planner approved either.

3.2 Proposed feedback sequence

Figure 2 arranges monitoring, diagnosis, planning, and approval as a Monitor–Analyze–Plan–Execute over Knowledge (MAPE-K) loop [8,9]. Only the planning step is exercised here, and it is exercised offline. The other three steps are drawn to show which observations and which human decisions a working system would have to supply.

3.3 Semantic representation and feasibility

The proposed material-planning workflow is organized through the semantic state representation in Eq. (1).

$$D(t) = \{G, S, P, U, R, C, H(t)\} \tag{1}$$

In Eq. (1), G denotes geometry and topology, S surface types, P physical parameters, U admissible actions, R predicted responses, C constraints, and H(t) the history of observations and decisions. This study evaluates the geometric inputs and the offline predictions; the observed history belongs to the operational extension. Equation (2) then attaches to each modeled surface its own geometry, material properties, and admissible actions.

$$\Sigma(G) = \{e_k\}, \qquad e_k = (g_k, \text{type}_k, p_k, u_k, c_k) \tag{2}$$

For surface k, g_k records area, height, and adjacency; type_k marks the surface as wall, roof, or pavement; p_k holds the material properties; u_k lists what may be assigned to it; and c_k records what may not. Three material genes per parcel across 63 parcels give 189 decision variables. Equation (3) defines the feasible design set,

$$\Omega = \{X \in U : g_j(X) \le 0, \quad j = 1, \ldots, 4\} \tag{3}$$

with four nonnegative constraint violations specified in Eqs. (3a)–(3b).

$$g_1(X) = \sum_{(i,j)\in E_{150}} \left[|\alpha_{w,i} - \alpha_{w,j}| - 0.30\right]_+$$

$$g_2(X) = \sum_i [\alpha_{w,i} - c_i]_+$$

$$g_3(X) = \sum_i 1\,[T_i^{\text{scr}} \notin [270, 370]] \frac{|T_i^{\text{scr}} - 330|}{100} \tag{3a}$$

$$g_4(X) = \sum_{i \setminus inD} [\alpha_{w,i} - 0.50]_+$$

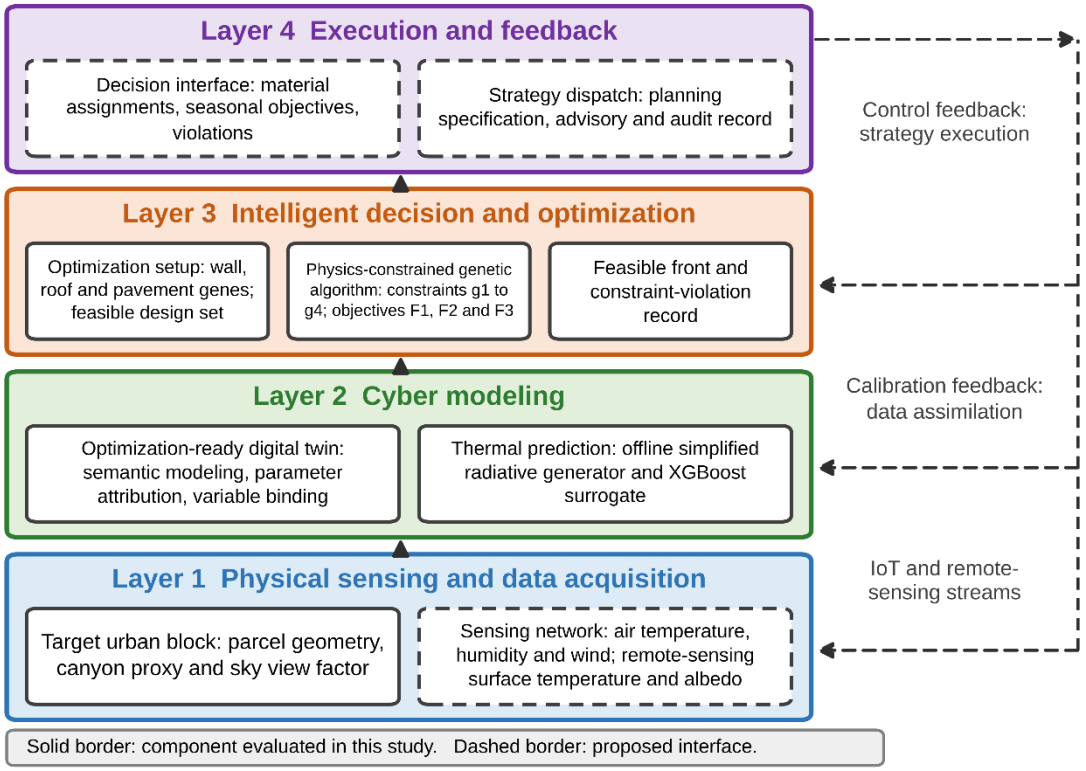


Figure 1. Urban representation and material-planning workflow; evaluated components are distinguished from proposed interfaces

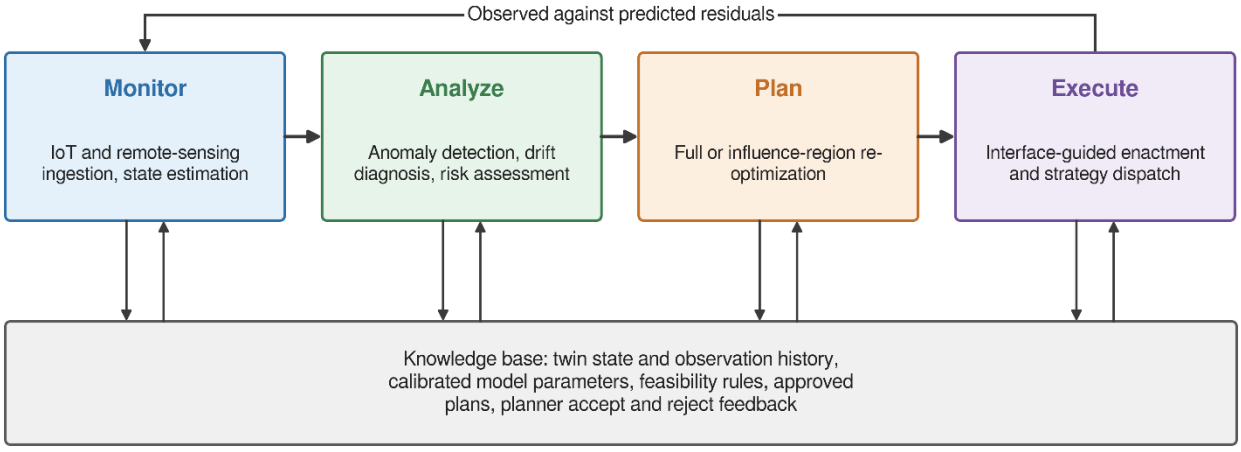


Figure 2. Feedback sequence surrounding the offline material-planning model

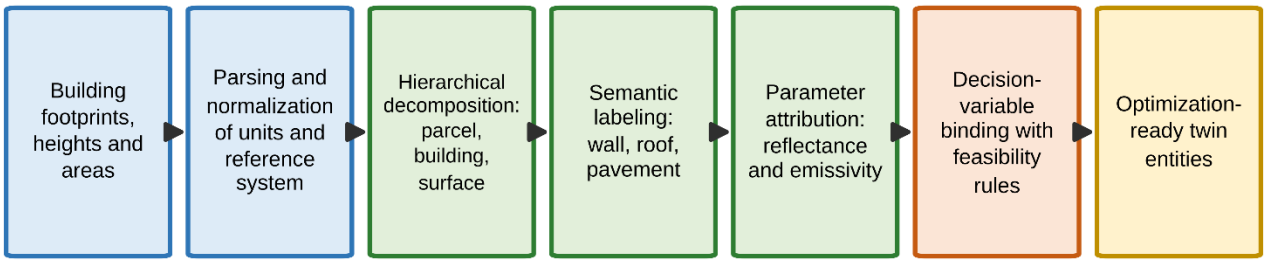


Figure 3. Binding parcel geometry to material options and feasibility records

$$c_i = \begin{cases} 0.25, h_i > 1.5, \\ 0.40, 1 < h_i \le 1.5, \\ 1.00, h_i \le 1. \end{cases}$$

$$T_i^{\mathrm{scr}} = \left(\frac{(1-\alpha_{\mathrm{eff},i})500 s_i + \varepsilon_{p,i} 400}{\varepsilon_{p,i}\sigma}\right)^{1/4} \tag{3b}$$

g1 limits how far adjacent wall reflectance may diverge, g2 imposes a reflectance ceiling that tightens with canyon geometry, g3 screens out radiating temperatures outside a physical band, and g4 adds a stricter wall threshold in the deep class. Only violations are counted, since the positive-part operator discards the slack. E150 holds the undirected centroid pairs within 150 m, and D is the deep geometry-proxy class, and the dimensionless ratio h_i is building height over the square root of projected footprint area. The fixed inputs of 500 and 400 W m−2 in Eq. (3b) serve the feasibility screen alone, and the temperature it returns is not the effective temperature of Eq. (5d). A solution counts as feasible only when all four violations are zero. Every method uses this same evaluator, with wall-material repair driven by numerical reflectance. These geometric classes are proxies; no street-canyon dimension was surveyed. Figure 3 shows how parcel geometry is bound to the material options and to the feasibility record.

3.4 Radiative model and material search

Each of the 63 parcels takes one of five wall materials, one of five roof materials, and one of four paving materials (Tables 1 and 2). Eleven of the fourteen reflectance–emissivity pairs come from measured LUMA samples [10], two from CRRC-rated white coatings identified by product number [11,12], and one from a measured Sedum roof [13]. Table 2 carries the source identifier for each. These are published optical analogs, so several limits follow. The green-roof option carries no evapotranspiration, the B001 paving record says nothing about permeability, and roof emissivity is listed in Table 2 but never enters the model. Relative material cost scores were drawn from indicative online retail listings such as Amazon and Taobao; because the quantities and specifications behind those listings do not match an installation here, F_3 is a comparative index with the standard materials scored zero. The nominal cost score is dimensionless, is given per material in Table 2, and is not a unit price. Neighborhood shortwave reflection is approximated by Eq. (4) rather than a geometry-resolved radiative exchange matrix.

$$K_{\mathrm{nb}} = 0.15\alpha_n I_d s, \qquad \alpha_n^{\mathrm{nom}} = 0.20 \tag{4}$$

The nominal neighbor reflectance α_n is 0.20 when a plan is evaluated and is varied when labels are generated. The 150 m centroid neighborhood is used by the adjacent-wall constraint alone. Neither building occlusion nor surface orientation is resolved by this approximation, and an independent comparison with SOLWEIG [14] would be needed to put a figure on the error. Shortwave, longwave, and MRT components are calculated using Eqs. (5a)–(5e).

$$\begin{aligned} K_{\downarrow} &= I_b\psi + I_d s + K_{\mathrm{nb}}, \\ K_{\uparrow} &= \alpha_{\mathrm{eff}} K_{\downarrow}, \\ \alpha_{\mathrm{eff}} &= 0.4\alpha_r + 0.6\alpha_p \end{aligned} \tag{5a}$$

$$K_{\mathrm{side}} = \frac{(1-s)K_{\downarrow}(1+\alpha_p)}{\max\{1-\alpha_w\alpha_p(1-s), 0.01\}} \tag{5b}$$

$$\begin{aligned} L_{\mathrm{sky}} &= \varepsilon_{\mathrm{sky}}\sigma T_a^4, \\ L_{\mathrm{wall}} &= \varepsilon_w\sigma T_w^4 + (1-\varepsilon_w)L_{\mathrm{sky}}, \\ L_{\downarrow} &= sL_{\mathrm{sky}} + (1-s)L_{\mathrm{wall}}. \end{aligned} \tag{5C}$$

$$\begin{aligned} Q_{\mathrm{abs}} &= \max\{(1-\alpha_{\mathrm{eff}})K_{\downarrow} + \varepsilon_{\mathrm{pav}}L_{\downarrow}, \\ &\qquad 0.5\varepsilon_{\mathrm{pav}}\sigma T_a^4\}, \\ T_s &= \left(\frac{Q_{\mathrm{abs}}}{\varepsilon_{\mathrm{pav}}\sigma}\right)^{1/4}, L_{\uparrow} = \varepsilon_{\mathrm{pav}}\sigma T_s^4. \end{aligned} \tag{5d}$$

$$\begin{aligned} S &= 0.70[0.06(I_d s + I_b\psi) + 0.06K_{\uparrow} + 0.22K_{\mathrm{side}}], \\ L &= 0.06L_{\mathrm{sky}} + 0.06L_{\uparrow} + 0.88L_{\mathrm{wall}}, \\ T_{\mathrm{mrt}} &= \left(\frac{S+0.97L}{0.97\sigma}\right)^{1/4} - 273.15 \end{aligned} \tag{5e}$$

Here, s is the ground SVF, I_β and I^d are the direct and diffuse shortwave irradiance, and α and ε are reflectance and emissivity, with the subscripts w, r and p marking wall, roof and pavement. Effective reflectance combines the roof and pavement values at weights of 0.4 and 0.6, a proxy for the surfaces facing the receptor. The model performs no full six-face radiative exchange calculation. T_s is accordingly an effective modeled radiating-surface temperature. Air and wall temperatures are in kelvin, and σ is the Stefan–Boltzmann constant. The wall term now includes reflected incident longwave, which corrects the low-emissivity imbalance in the earlier version. The sun-exposure switch ψ is one when I_β exceeds 10 W m^{-2} and s exceeds 0.2, and zero otherwise, and it does not resolve solar azimuth or directional shading. Within these assumptions, Eq. (5e) returns MRT in degrees Celsius. Equation (5f) then defines the three objectives minimized during the material search.

$$\begin{aligned} F_1(X) &= \frac{1}{N}\sum_i \hat{T}_{i,\mathrm{sum}}(X), \\ F_2(X) &= -\frac{1}{N}\sum_i \hat{T}_{i,\mathrm{win}}(X), \\ F_3(X) &= \frac{\sum_i A_i\kappa_i(X)}{\sum_i A_i}, \\ \kappa_i(X) &= 0.3c_w(w_i) + 0.4c_r(r_i) + 0.3c_p(p_i). \end{aligned} \tag{5f}$$

Here N = 63 and the hatted temperatures are the seasonal surrogate predictions. F_1 minimizes summer MRT, F_2 minimizes negative winter MRT, and F_3 measures nominal intervention cost. Each area A_i is a projected parcel footprint in EPSG:32651, and the material scores follow Table 2. The 0.3/0.4/0.3 surface shares stand in for installation areas that were not available, so F_3 cannot be read as money.

The physics-constrained genetic algorithm (PC-GA) and NSGA-II each run 60 individuals over 80 generations, and the F_1-only simulated annealer is given the same 4,860 evaluations. Every method is repeated with 30 seeds. PC-GA, NSGA-II, and the annealer share the g_1–g_4 evaluator and the repair procedure. The penalty GA starts from 60 feasible individuals and uses the same one-point crossover and 5% gene mutation as NSGA-II, but it never repairs an offspring. It adds 20 times the total constraint violation to each normalized objective before nondominated sorting, which tests a different way of handling the same constraints at the same budget.

Table 1. Material decisions and geometric feasibility rules

Decision or test	Implemented meaning	Limit or status
Wall gene	One of five wall materials per parcel	Reflectance 0.17–0.81
Roof gene	One of five roof materials per parcel	Reflectance 0.07–0.84
Pavement gene	One of four paving materials per parcel	Reflectance 0.10–0.42
g1 adjacent contrast	Wall reflectance difference within 150 m	At most 0.30
g2 canyon ceiling	Wall reflectance by geometry proxy	≤0.25 if h>1.5; ≤0.40 if 1<h≤1.5
g3 temperature screen	Fixed-input radiative feasibility screen	270–370 K
g4 deep canyon rule	Wall rule in deep proxy class	Wall α≤0.50 in deep class

Table 2. Published optical analogs and nominal cost scores for the 14 planning categories. W, R, and P denote wall, roof, and paving. Sample and product IDs identify the underlying records, which are not local installations

Surface and material	α	ε	Nominal cost score
W1 Brick B007	0.22	0.94	0
W2 Light paint B012	0.56	0.95	15
W3 White coat W125-0001	0.81	0.89	35
W4 Dark brick B005	0.17	0.94	5
W5 Metal Z002	0.25	0.16	80
R1 Asphalt A007	0.07	0.93	0
R2 Cool coat 0772-0065	0.84	0.88	40
R3 Sedum	0.16	1.00	60
R4 Concrete C004	0.37	0.95	10
R5 Metal Z001	0.36	0.58	50
P1 Asphalt A010	0.10	0.96	0
P2 Light concrete C006	0.42	0.95	20
P3 Permeable B001	0.30	0.94	30
P4 Granite G005	0.22	0.89	10

3.5 Surrogate training and blocked validation

For each season q, the surrogate approximates the radiative generator response under the synthetic meteorological forcing and parameter perturbations used for label generation:

$$R_q = M(F_q, X, G; \theta), \quad \hat{R}_q = \hat{M}_q(X, G; \beta) \approx \mathbb{E}[R_q \mid X, G] \tag{6}$$

Here F^{φ} is the synthetic meteorological forcing, X the material configuration, G the parcel geometry, θ the radiative-model parameters, and β the fitted surrogate parameters. Trained under squared error, the surrogate approximates the conditional mean of the simulated responses inside the training distribution. Extreme Gradient Boosting (XGBoost) takes material properties, geometric descriptors, SVF, and neighborhood features, and it is given no day-specific meteorological variable, so Eq. (6) says nothing about generalization to unseen weather days. We regenerated 37,800 synthetic labels from 200 material-sample identifiers, three perturbation repeats, and 63 parcels, using the corrected ground SVF and the source-linked material library of Table 2, and kept the sample ordering while the optical features and thermal responses were updated. XGBoost used 240 trees, maximum depth 6, learning rate 0.07, subsample 0.85, and column subsample 0.90, with seed 42. Validation went beyond a random 80/20 split to five contiguous east–west spatial holdouts and a 20% material-identifier holdout, which are the splits that test spatial and material transfer. Every error quoted measures agreement with the simplified radiative generator, which is the only ground truth available here. Figure 4 sets out the prediction interface and these splits.

3.6 Assimilation specification

A future operational system could assimilate sensor observations to update the modeled thermal state through the following correction equation:

$$s_t^+ = s_t^- + K_t[z_t - h(s_t^-)] \tag{7}$$

Here s_t^- and s_t^+ are the prior and updated states, z_t the observation vector, h the observation operator, and K_t the assimilation gain [7, 15]. No sensor time series was available, so neither the gain nor the accuracy of the update is evaluated here, and Eq. (7) stands as an interface specification. Figure 5 sets out the observation-update sequence it would belong to.

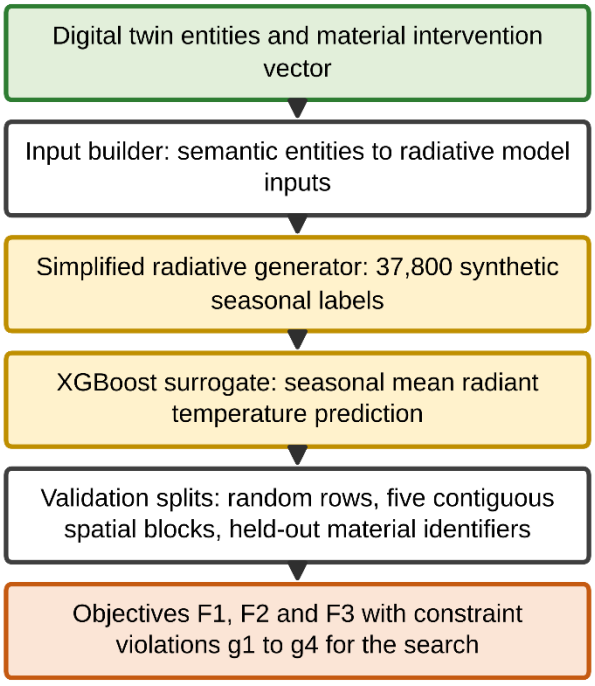


Figure 4. Surrogate prediction interface and validation against synthetic radiative labels

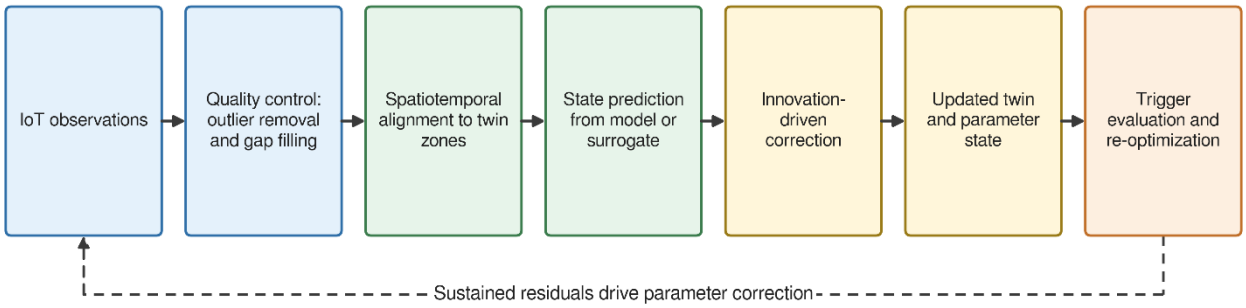


Figure 5. Proposed observation-update workflow

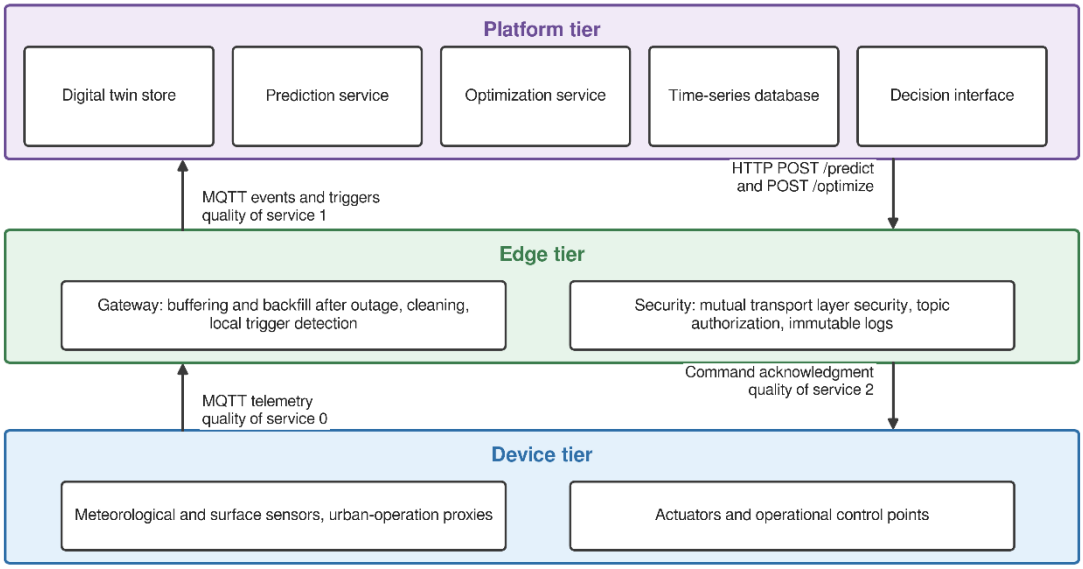


Figure 6. Device, edge, and platform interfaces proposed for a later deployment

3.7 Proposed communication interface

Figure 6 gives the Message Queuing Telemetry Transport (MQTT) interface proposed for Internet of Things (IoT) sensor observations, system events, and prediction requests [16]. The Hypertext Transfer Protocol (HTTP) requests drawn in Figure 6 are design placeholders for a later service implementation and not measured endpoints. Authentication, delivery, retry, and latency would all have to be validated in operation. The timing results reported below cover local model computation alone, with no network transmission and no system-level communication overhead.

3.8 Trigger and stability specification

A future operational system could incorporate risk, prediction-drift, and feasibility triggers, defined as follows:

$$T_{\text{risk}}(t) = 1\{\sum_{i\in\mathcal{Z}} w_i \, 1[R_{i,t} > R^*] > \tau_{\text{risk}}\} \quad (8)$$

$$T_{\text{drift}}(t) = 1\left\{\frac{1}{W}\sum_{k=0}^{W-1} \delta_{z,t-k} > \tau_{\text{drift}}\right\} \quad (9)$$

$$T_{\text{feas}}(t) = 1\{\Omega_t \neq \Omega_{t-1} \ \vee \ B_t < B^*\} \quad (10)$$

In Eqs. (8) to (10), $R_{i,t}$ is the vulnerability-weighted risk, w_i the exposure weight, δ the prediction residual, W the moving-window length, Ω the feasible design set, and B the available budget, and the indicator function returns one when its condition holds.

The candidate influence region is the same 150 m neighborhood used elsewhere. Risk thresholds, residual limits, and exposure weights would have to be calibrated against observed and stakeholder data before any of this fired.

$$\Delta(X, X^{\text{prev}}) = \sum_k 1\{x_k \neq x_k^{\text{prev}}\} \quad (11)$$

The change count Δ counts how many material assignments differ between successive plans, and it is the quantity a stability regularizer would act on. Whether it would hold a plan steady can only be answered with time-stamped observations and repeated optimization events. Figure 7 places the triggers and the change count in the review and dispatch sequence.

3.9 Decision interface specification

A decision interface would show the material assignment, the predicted summer and winter MRT, the nominal cost index, and any constraint violations. The normalized-ideal solution is kept here only as a representative Pareto member, because direct radiative evaluation puts it 0.222 °C warmer in summer than the standard materials once ground SVF is corrected. We therefore carry forward a preselected summer-oriented solution together with one whose winter MRT reduction is smaller. Neither is offered as a universally optimal plan; the

pair shows how seasonal performance trades against intervention cost.

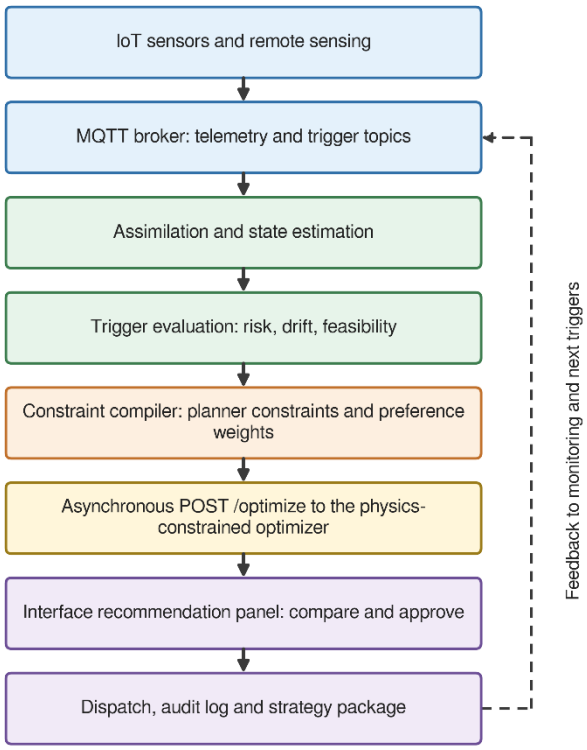


Figure 7. Proposed trigger, review and dispatch sequence

3.10 Site, data and rerun protocol

The static case covers 63 building footprints around 31.1945° N, 121.4365° E in Xujiahui, Shanghai, China; their projected area totals 63,344.95 m^2. Heights are completed or estimated values (mean 28.75 m; range 13.7–74.9 m). A 1 m digital surface model (DSM) raster produced by extruding the footprints supports a 36-direction, 100 m horizon scan. The original centroid-ring receptor largely sampled building pixels: 61 of 63 rings contained a majority of such pixels. We therefore sampled 2,520 raster ground pixels 1–6 m outside the footprints, obtaining a parcel-mean solid-angle SVF of 0.409 rather than the archived 0.892. The alternative receptor is reproducible in the supplied geometry but has not been aligned with surveyed pedestrian locations. Only 1,136 points have a complete 100 m raster window; horizon estimates near the raster edge remain uncertain. The canyon proxy is computed from building height divided by the square root of footprint area, not from surveyed street width. We use its shallow, medium, and deep classes only for geometry-conditioned constraints and error summaries. The exterior-ground SVF samples and the original raster are available from the corresponding author on request.

4. Results and discussion

4.1 Corrected labels and surrogate transfer

After the ground receptor was corrected, the wall longwave balance repaired, and the source-linked optical inputs substituted, the 37,800 summer labels ranged from 38.933 to 71.853 °C, with a mean of 59.884 °C, and none fell below 15 °C. Table 3 reports a summer root mean square error (RMSE) of 0.848 °C on random rows, 0.495 to 1.043 °C across the five spatial holdouts, and 1.240 °C when whole material-sample identifiers are held out, the last of these keeping every repeat from a given sample on the same side of the split. Each target is a synthetic radiative calculation, so the errors measure agreement with the generator and nothing beyond it. Stratifying that material holdout by canyon proxy gives a summer RMSE of 1.164 °C in the shallow group, 1.155 °C in the medium group, and 1.432 °C in the deep group. The deep group is the hardest of the three, as greater geometric complexity would predict, though the proxy classes are not measurements of canyon width.

4.2 Feasible search and seasonal trade-offs

Over 30 seeds at 4,860 evaluations per run, the lowest-summer-F_1 member of each final feasible front averaged 55.703 ± 0.253 °C for PC-GA, 58.386 ± 0.276 °C for NSGA-II and 58.868 ± 0.251 °C for the penalty GA. The F_1-only annealer reached 58.492 ± 0.219 °C without producing a three-objective front. PC-GA therefore reached the lowest mean summer objective and kept its multi-objective alternatives. These are surrogate objectives; Table 4 reports what direct evaluation makes of the same plans. A uniform-material reference gives the search one more thing to be measured against. Assigning bare-metal walls, white cool roofs and asphalt pavement to every parcel satisfies the implemented constraints and returns a direct summer F_1 of 55.088 °C, a winter F_2 of −20.382 °C and an F_3 of 40, but the winter cost of that plan is a 4.958 °C reduction in winter mean radiant temperature against the standard-material reference, where the summer-oriented plan in Table 4 costs 1.819 °C. Its facade retrofit extent is also unverified. It marks a theoretical boundary, and the PC-GA member is not claimed as a global summer minimum. One further caution belongs here. The surrogate endpoints quoted above sit below the direct-model values for the corresponding plans in Table 4, by more than the holdout errors in Table 3 would allow. Minimizing a fitted response surface selects the points where that surface happens to be biased low, which is why every outcome reported below comes from direct radiative evaluation.

Normalized three-objective hypervolume across the same 30 seeds was 0.592 for PC-GA, 0.545 for NSGA-II, and 0.486 for the penalty GA, computed on common objective limits with the reference point (1.1, 1.1, 1.1). PC-GA thus achieved the highest mean hypervolume and the lowest mean sum of endpoint values at this budget.

Table 3. XGBoost agreement with the simplified radiative generator after ground-SVF correction

Validation split	Summer RMSE °C	Summer R^2	Winter RMSE °C	Winter R^2
Random rows	0.848	0.964	0.681	0.961
Five spatial blocks	0.495–1.043	0.932–0.989	0.455–0.758	0.944–0.985
Held-out material IDs	1.240	0.918	1.255	0.859

Table 4. Direct-model responses of representative feasible plans over 30 common synthetic forcing realizations. A negative summer gain denotes warming; F_2 is minus winter MRT

Direct-model plan	F1 summer °C	F2 winter °C	F3 index	Summer gain °C
Standard materials	59.914	−25.340	0.00	reference
Low-cost member	60.474	−25.674	3.78	−0.560
Normalized-ideal member	60.136	−25.308	9.88	−0.222
Summer-oriented member	58.429	−23.521	30.63	1.484
Smaller seasonal-shift member	59.654	−24.824	20.33	0.260

The penalty GA did reach feasible final members, but only 28.73% of the candidates it evaluated along the way were feasible. On the PC-GA fronts, about 10.1% of the wall genes subject to the g_2 limit lay exactly on it, a pattern that reflects the discrete material ladder as much as the constraint. These comparisons hold for the present surrogate and constraint set at this evaluation budget.

Direct radiative evaluation reverses the ranking for two of the candidates. Against standard materials, the normalized-ideal solution is 0.222 °C warmer in summer and the low-cost solution 0.560 °C warmer. We therefore use a summer-oriented Pareto solution to show the cooling potential: it reduces summer MRT by 1.484 °C, with a paired 95% confidence interval of 1.379 to 1.590 °C, at the cost of a 1.819 °C reduction in winter MRT and a nominal F_3 of 30.63. A second Pareto solution trades less in both directions, cooling summer by 0.260 °C and winter by 0.516 °C for an F_3 of 20.33. Of the 60 feasible Pareto solutions obtained with seed 0, 36 reduce summer MRT, and 29 of those reach at least 0.2 °C of modeled cooling. Not one improves summer and winter together, which is the seasonal trade-off this problem cannot escape.

These values need to be set against the published record, which points the other way. Field measurement over a solar-reflective road coating in Los Angeles found mean radiant temperature 4 °C higher at midday than over uncoated asphalt concrete [17], and a neighborhood simulation of the same city reported increases above paved surfaces of up to about 7.8 °C when pavement reflectance was raised by 0.3, with physiological equivalent temperature at unshaded receptors rising by 2.2 °C [18]. Those are receptor values at pedestrian height for one surface class, and the objectives here are parcel means in which wall, roof and pavement change together, so the magnitudes are not comparable. The direction, however, is reproduced: raising pavement reflectance raises modeled MRT in this model too, because the reflected shortwave reaching the receptor through Eqs. (5a) and (5b) grows faster than the effective surface temperature of Eq. (5d) falls. The summer gains reported above therefore do not come from reflectance at all. The wall longwave term carries a weight of 0.88 in Eq. (5e), so facade emissivity governs the receptor's longwave load, and a low-emissivity facade lowers that load without incurring the reflected shortwave penalty that a bright surface brings. The published studies raised albedo and left facade emissivity alone. They test a different intervention.

4.3 Direct assessment and SVF sensitivity

Each candidate and the standard-material baseline were evaluated under the same corrected radiative model and the same 30 shared synthetic forcing realizations, with ground SVF perturbed identically inside each paired comparison.

Widening the horizon scan to 150 m left the summer-oriented plan cooling by 1.461 °C. Moving the ground receptors out to between 6 and 12 m beyond the building footprints raised that figure to 1.596 °C, and an alternative projected-sky weighting gave 1.618 °C. This last case tests the weighting assumption alone. All 63 parcel-level SVF values were then allowed to move independently by ±0.10 around their baselines. A worst-case search on a 0.001 SVF grid returned summer cooling between 1.274 and 1.738 °C for the summer-oriented plan, and between 0.022 and 0.520 °C for the smaller seasonal-shift plan. Across three assumed SVF error distributions at 5,000 draws each, the summer-oriented plan never lost its modeled cooling. Under some SVF configurations, a different fixed Pareto member did perform better. The direction of the cooling therefore survives this test; the layout that delivers it does not. A matched timing test on an Intel Core i7-9850H ran 50 plans, each of 63 parcels, under two synthetic 24-hour forcing profiles. Direct radiative evaluation averaged 76.1 ms per plan against 2.03 ms for surrogate inference, a 37.5-fold speedup per query. The figure excludes synthetic-label generation, surrogate training, geometry preprocessing, and platform communication, so it is not an end-to-end acceleration. It also depends on how the direct model is written, since evaluating the same expressions for all parcels at once instead of parcel by parcel lowers the direct cost substantially.

4.4 Material availability and re-optimization

To see whether a plan can be adapted when a material becomes unavailable, the white cool-roof option was withdrawn, and a repaired incumbent plan was compared with a fresh start across 30 paired simulated-annealing runs of 4,860 evaluations each. At 500 evaluations, the incumbent start held a mean F_1 of 58.525 °C against 60.382 °C for the fresh start, but by the end the two had converged to 55.680 and 55.723 °C. The early advantage shows through as a better starting point, and the final figures show no sustained gain in convergence. The experiment does establish that re-optimization under a changed material set is feasible, which is a precondition for observation-driven optimization.

4.5 Limitations and scope of inference

The ground-receptor ring is a sampling proxy; no pedestrian path was surveyed, and some horizon scans reach the raster boundary. The SVF sensitivity analysis covers receptor placement, horizon radius, sky weighting, and parcel-level variation, but leaves untouched the uncertainty in building height, in vegetation, and in the radiative model itself. The published optical analogs make the parameters traceable without making them site-specific, and surface finish and weathering will move them. The green-roof model has no evapotranspiration. A uniform bare-metal-wall and

cool-roof plan achieves more modeled summer cooling than any plan reported here, at a larger winter cost and with its constructability unverified. F_3 is a nominal index, and the speedup excludes data generation, training, and communication. Observation-driven feedback was not implemented. One simplification bounds the central result: Eq. (5c) lets a low-emissivity facade reflect only sky longwave, whereas a facade in a real canyon also reflects the warmer ground and the facing wall, so the modeled benefit of low-emissivity surfaces is an upper bound. The model also omits directional shading, building occlusion, and multiple inter-reflection inside canyons, which puts the largest approximation error in the deep geometry-proxy class; a paired comparison against SOLWEIG [14] on the same geometry is the direct way to measure that bias. Independent MRT measurement or detailed radiative-model comparison is needed before any of this is read as site-level thermal performance.

5. Conclusion

This study built a geometry-linked material-planning framework and tested its static optimization core across 63 parcels in Xujiahui. The revised analysis rests on 14 source-linked optical material pairs, a corrected ground-receptor SVF, and a wall longwave balance that now includes reflected incident radiation. Under shared synthetic forcing, a summer-oriented feasible solution cut modeled summer MRT by 1.484 °C, at a winter cost of 1.819 °C and a nominal cost index of 30.63. The cooling stayed positive across every receptor configuration tested and held above 1.274 °C when parcel-wise SVF was varied by ±0.10. Constrained material optimization is therefore workable at this scale, and the seasonal trade-off is part of what it returns. Validation against observed thermal conditions is the next step; sensor assimilation and operational feedback remain to be built.

Acknowledgements

The authors acknowledge Batangas State University and the National Engineering University for institutional support during the preparation of this work.

Ethical issue

The authors are aware of and comply with best practices in publication ethics, specifically with regard to authorship (avoidance of guest authorship), dual submission, manipulation of figures, competing interests, and compliance with policies on research ethics. The authors adhere to publication requirements that the submitted work is original and has not been published elsewhere.

Data availability statement

The manuscript contains all the data. However, additional data will be provided by the corresponding author upon reasonable request.

Conflict of interest

The authors declare no potential conflict of interest.

References

[1] Z. Li, X. Wang, H. Zhao and X. Xu, "Spatiotemporal patterns of the evolution of the urban heat island effect and population heat exposure risks in Xi'an, one of China's megacities, from 2003 to 2023," Land, vol. 14, no. 10, article 2021, 2025. DOI: https://doi.org/10.3390/land14102021.

[2] T. Yang, G. Li and G. Xu, "Urban street canyon morphology and its effect on climate-responsive outdoor thermal environment in severe cold regions: a case study of Hohhot, China," International Journal of Biometeorology, vol. 69, no. 5, pp. 1043-1055, 2025. DOI: https://doi.org/10.1007/s00484-025-02877-9.

[3] P. M. Cuce, E. Cuce and M. Santamouris, "Towards sustainable and climate-resilient cities: mitigating urban heat islands through green infrastructure," Sustainability, vol. 17, no. 3, article 1303, 2025. DOI: https://doi.org/10.3390/su17031303.

[4] V. P. Lopez-Cabeza, M. Videras-Rodriguez and S. Gomez-Melgar, "An open-source urban digital twin for enhancing outdoor thermal comfort in the city of Huelva (Spain)," Smart Cities, vol. 8, no. 5, article 160, 2025. DOI: https://doi.org/10.3390/smartcities8050160.

[5] Z. Zhao, H. Li and S. Wang, "Surrogate-assisted coordinated design optimization of building and microclimate considering their mutual impacts," Applied Energy, vol. 383, article 125374, 2025. DOI: https://doi.org/10.1016/j.apenergy.2025.125374.

[6] Z. Zhao, H. Li and S. Wang, "Machine learning-based surrogate models for fast impact assessment of a new building on urban local microclimate at design stage," Building and Environment, vol. 266, article 112142, 2024. DOI: https://doi.org/10.1016/j.buildenv.2024.112142.

[7] Y. Cui, M. Chu, Z. He, J. Albertson, Z. Wang and Q. Li, "Estimating anthropogenic heat flux by assimilating meteorological observations with a Kalman filter approach," Philosophical Transactions of the Royal Society A, vol. 383, no. 2308, article 20240572, 2025. DOI: https://doi.org/10.1098/rsta.2024.0572.

[8] J. O. Kephart and D. M. Chess, "The vision of autonomic computing," Computer, vol. 36, no. 1, pp. 41-50, 2003. DOI: https://doi.org/10.1109/MC.2003.1160055.

[9] R. Ben Halima, M. Hachicha, A. Jemal and A. Hadj Kacem, "MAPE-K patterns for self-adaptation in cyber-physical systems," The Journal of Supercomputing, vol. 79, no. 5, pp. 4917-4943, 2023. DOI: https://doi.org/10.1007/s11227-022-04828-2.

[10] S. Kotthaus, T. E. L. Smith, M. J. Wooster and C. S. B. Grimmond, "Derivation of an urban materials spectral library through emittance and reflectance spectroscopy," ISPRS Journal of Photogrammetry and Remote Sensing, vol. 94, pp. 194-212, 2014. DOI: https://doi.org/10.1016/j.isprsjprs.2014.05.005.

[11] Cool Roof Rating Council, "Rated Roof Products Directory," 2026. [Online]. Available: https://coolroofs.org/directory/roof [Accessed 1 November 2026].

[12] NOROO Paint & Coatings, "CRRC notification of product rating: Energy Saver Cool Wall White, W125-0001," 2023. [Online]. Available: https://www.noroopaint.com/inc/filedown2.asp?fileloc=%2Ffile%2Fprod_file%2F&filenm=W125-0001+CRRC+Wall+Notification+of+Product+Rating_2023-03-13.pdf&savefilenm=W125-0001+CRRC+Wall+Notification+of+Product+Rating_2023-03-13.pdf [Accessed 1 November 2026].

[13] C. Feng, C. C. Wu and Q. L. Meng, "Experimental study on the radiative properties of a Sedum lineare greenroof," Applied Mechanics and Materials, vols. 174-177, pp. 1986-1989, 2012. DOI: https://doi.org/10.4028/www.scientific.net/AMM.174-177.1986.

[14] F. Lindberg, B. Holmer and S. Thorsson, "SOLWEIG 1.0 – modelling spatial variations of 3D radiant fluxes and mean radiant temperature in complex urban settings," International Journal of Biometeorology, vol. 52, no. 7, pp. 697-713, 2008. DOI: https://doi.org/10.1007/s00484-008-0162-7.

[15] R. E. Kalman, "A new approach to linear filtering and prediction problems," Journal of Basic Engineering, vol. 82, no. 1, pp. 35-45, 1960. DOI: https://doi.org/10.1115/1.3662552.

[16] OASIS, "MQTT Version 5.0," OASIS Standard, 2019. [Online]. Available: https://docs.oasis-open.org/mqtt/mqtt/v5.0/mqtt-v5.0.html [Accessed 26 October 2026].

[17] A. Middel, V. K. Turner, F. A. Schneider, Y. Zhang and M. Stiller, "Solar reflective pavements – a policy panacea to heat mitigation?," Environmental Research Letters, vol. 15, no. 6, article 064016, 2020. DOI: https://doi.org/10.1088/1748-9326/ab87d4.

[18] M. Taleghani, D. Sailor and G. A. Ban-Weiss, "Micrometeorological simulations to predict the impacts of heat mitigation strategies on pedestrian thermal comfort in a Los Angeles neighborhood," Environmental Research Letters, vol. 11, no. 2, article 024003, 2016. DOI: https://doi.org/10.1088/1748-9326/11/2/024003.



This article is an open-access article distributed under the terms and conditions of the Creative Commons Attribution (CC BY) license (https://creativecommons.org/licenses/by/4.0/).